JMEPEG (2008) 17:115–122
DOI: 10.1007/s11665-007-9117-0

1059-9495/$19.00

# Controlling End-Grain Corrosion of Austenitic Stainless Steels

*Kamlesh Chandra, Vivekanand Kain, and Puppala Ganesh*

*(Submitted August 10, 2006; in revised form February 22, 2007)*

**SS 304L is widely used as a structural material in applications handling nitric acid such as nuclear fuel processing plants and nuclear waste management facilities. Bar, wire, and tubular products of this material are especially susceptible to end-grain corrosion in nitric acid environment. Such an attack takes place on the tubular and forged surfaces that are perpendicular to the hot-working direction and occurs as localized pitting type attack. This study shows that the possible reasons for the directional nature of end-grain attack are the manganese sulfide inclusions aligned along the hot-working direction and/or segregation of chromium along the flow lines during the fabrication stage itself. It has been shown in this study that controlled solution annealing, laser surface remelting, and weld overlay can be used to avoid/minimize end-grain corrosion. Different annealing heat-treatments were carried out on two heats of SS 304L tube and susceptibility to corrosion was measured by ASTM A 262 practice C and electrochemical potentiokinetic reactivation (EPR) test. Solution annealing at 950 °C for 90 min has been shown to increase the resistance to end-grain corrosion. Laser surface remelting using continuous wave $CO_2$ laser under argon shield and weld deposition (overlay) using SS 308L material were done on the end faces of the tubes. These samples were completely resistant to end-grain corrosion in nitric acid environments.**

**Keywords** austenitic stainless steel, end-grain corrosion, laser surface remelting, nitric acid service, weld overlay

## 1. Introduction

Austenitic stainless steels are extensively used in nuclear, chemical, and other industries due to their unique combination of corrosion resistance, fabricability, weldability, and mechanical properties. Although these steels have good resistance to general corrosion owing to the formation of a thin chromium rich passive surface film (Ref 1-3), they are susceptible to localized corrosion attack such as pitting, intergranular corrosion (IGC), and stress corrosion cracking. These stainless steels are prone to sensitization—a process by which chromium carbides form at grain boundaries with adjacent regions depleted of chromium (Ref 1-3). This happens at the temperature range of 500-850 °C such as during welding. Sensitization is the basic reason for IGC and intergranular stress corrosion cracking (IGSCC). One of the methods to overcome sensitization in austenitic stainless steels is to lower the carbon content below 0.02 wt.% (Ref 1-2). Low-carbon grade stainless steel (SS) 304L is one of the structural materials particularly suited to nitric acid environments. It has been shown that apart from carbon content, chromium, and nickel content of the stainless steel determines its susceptibility to sensitization and IGC (Ref 4). The nuclear fuel processing plants and nuclear waste management facilities use nitric acid of varying concentrations and at temperatures up to 110 °C. The process equipments, pipings, and components for these facilities are made up of mainly SS 304L materials.

The IGC of stainless steels in nitric acid environments due to sensitization (as a result of welding during fabrication) can be minimized (Ref 5-8) by use of sensitization resistant materials, e.g., Nitric Acid Grade (NAG) stainless steel. The very low-carbon grade of SS 304L is also susceptible to corrosion attack in nitric acid environment in highly oxidizing conditions generated either by high temperatures or in the presence of dissolved corrosion products such as $Fe^{+3}$ and $CrO_4^{2-}$ ions. These high-valence oxidizing ions may be accumulated due to the uniform corrosion of stainless steel tanks used for the storage of nitric acid over a long-period of time. Another form of corrosion to which particularly bar, wire, and tubular products of stainless steels are susceptible to attack in nitric acid environment, is end-grain corrosion. It takes place on the tubular and forged surfaces that are perpendicular to hot-working direction and occurs as localized pitting like attack that develop along the hot-working direction and finally the corrosion occurs as intergranular attack (Ref 5, 7-10). It has been identified (Ref 8) as a major form of corrosion in those components in which cross-sectional surfaces are exposed to the oxidizing process fluid. In reprocessing plants that use sensitization resistant stainless steels (L grade or NAG grade stainless steels), end-grain corrosion is shown to be a major degradation mode in components such as instrument tubing and tube to tube sheet welds. Forgings and set in pipe branches are also reported (Ref 7) to be affected by end-grain corrosion. Exposure studies done in a dissolver in a reprocessing plant (in vapor phase) showed very heavy corrosion rates of 0.2-0.6 mm/year even for NAG grade of stainless steel and this was attributed mainly to end-grain corrosion (Ref 7).

**Kamlesh Chandra** and **Vivekanand Kain,** Materials Science Division, Bhabha Atomic Research Centre, Trombay, Mumbai 400 085, India; and **Puppala Ganesh,** Raja Ramanna Centre for Advanced Technology, Indore 452 013, India. Contact e-mail: kchandra@barc.gov.in.

The directional nature of end-grain attack has been explained by the dissolution of aligned sulfide inclusions along the hot-working direction (Ref 5-11). Segregation of phosphorous, chromium and silicon along the flow lines during the fabrication stage is another mechanism for end-grain corrosion (Ref 5, 9-13). The end-grain corrosion of a material is related to the defect in manufacturing and processing stage such as a high-inclusion content in the material or use of an improper solution annealing heat treatment. Instead of discarding these defective materials against end-grain corrosion, some suitable methods can be used to avoid or minimize such type of attack. These methods may include solution annealing to homogenize the chemical composition, laser surface remelting of the end faces, surface alloying by melting additional chromium or molybdenum on the surface layer, cladding with SS 310 (Ref 11), weld deposition with SS 308L or welding a better quality material of the same grade on the end faces. Jeng et al. (Ref 11) has shown that laser surface remelting effectively prevents the continued propagation of end-grain corrosion in SS 347 exposed to nitric acid. Laser melting also eliminates the sensitization in the surface layer of SS 304L and also prevents the continuation of intergranular attack by nitric acid on previously corroded surfaces. In an early work of Stewart et al. (Ref 12), it has been shown that the laser surface melting markedly improves the pitting resistance of type 304L stainless steel. Laser surface remelting on the surface layer of the sensitized SS 321 has also been shown to improve the resistance to pitting and IGC (Ref 13).

There is limited literature available on the exact reason or mechanism for the occurrence of end-grain corrosion in austenitic stainless steels. In this study, we have investigated the possible reasons for end-grain attack in SS 304L pipes and different methods to minimize or avoid this type of attack. Controlled solution annealing, laser surface remelting and weld deposition of SS 308L over the end faces of tubes are the three remedial methods that were used.

## 2. Experimental Procedures

### 2.1 Materials and Heat Treatment

Two heats of SS 304L material numbered A (low carbon) and B (medium carbon) were studied. Both the heats were in pipe form, O.D. 33.4 mm, and wall thickness 3.05 mm. The chemical compositions of both the heats are given in Table 1. These materials were in the solution-annealed condition and showed step structure. Samples of dimension 15 mm width and 10 mm length were cut from the pipes of heat A and B and sealed separately in quartz tubes under argon atmosphere at 0.1 mm Hg pressure. These sealed samples were subjected to solution annealing heat treatment at 950 °C for 30 and 90 min, respectively, and at 1000 °C for 30 min followed by water quenching.

### 2.2 Microstructural Characterization

The microstructures of both the heats of SS 304L samples were examined using an optical microscope after electrochemical etching in oxalic acid according to ASTM A 262 practice A (Ref 14). The microstructures were examined on both the longitudinal and transverse sections of the samples.

### 2.3 Single Loop Electrochemical Potentiokinetic Reactivation Test

The single loop electrochemical potentiokinetic reactivation test (SL-EPR) (Ref 15, 16) was conducted to assess the degree of sensitization (DOS) of stainless steels. The test was carried out in a solution of 0.5 M $H_2SO_4$ + 0.01 M KSCN (deaerated) at room temperature. After holding the specimen in the passive region at +200 mV (SCE) for 2 min, the electrochemical potential was reverse scanned to the open circuit potential at a scan rate of 100 mV/min. The $P_a$ value of the specimen was taken as a measure of DOS which was calculated by the formula:

$$P_a = Q/\mathrm{GBA},$$

where $Q$ = total charge for the reactivation loop (in Coulombs), GBA: grain boundary area = $A_s \times 5.0954 \times 10^{-3}$ exp(0.3469$X$), $A_s$ = Specimen area (in $cm^2$), and $X$ = ASTM grain-size number as per A 112.

### 2.4 Laser Treatment

Rings of length 20 mm were cut from both the pipes. Laser surface remelting was conducted on both the end faces of these rings using continuous wave $CO_2$ laser under argon shield. About 1 mm thickness of the material on each end face was melted using the laser. Trials were made with different laser powers and velocities. Based on examination of the laser surface-melted surfaces, an optimum laser power and velocity were selected that did not result in surface cracks on the remelted regions. Therefore, the laser beam power and its velocity were maintained at 2.4 kW and 9.4 mm/s, respectively. To examine the microstructure of the laser-remelted samples, the ring was cut and the longitudinal section was polished and etched in 10% oxalic acid solution.

### 2.5 Weld Overlay

A ring of length 15 mm was cut from the pipe of heat A. Weld deposition of about 1 mm depth was carried out on both the end faces of the ring sample using weld filler material SS 308L (composition in wt.%: C-0.03, Cr: 19.5-22.0, Ni: 9.0-11.0, Mn: 0.25-0.6, Si: 0.3, S: 0.03, P: 0.03, single values indicate maximum values). The microstructure of the weld deposited sample was obtained after examining the longitudinal section of the ring. The voltage and current during the welding process were monitored and were 18 V and 70 A.

**Table 1 Chemical composition (wt.%) of 304L stainless steel**

| Heat code | C | Si | Mn | P | S | Ni | Cr |
|---|---|---|---|---|---|---|---|
| A | 0.015 | 0.51 | 1.59 | 0.03 | 0.02 | 11.23 | 19.07 |
| B | 0.030 | 0.45 | 1.40 | 0.03 | 0.02 | 11.08 | 18.50 |

### 2.6 Ferrite Meter Measurement

The δ-ferrite formed after laser surface remelting of the samples was measured by a ferrite meter. The conversion from the ferrite number measured from the ferrite meter to percentage ferrite (magnetic phase) was done using the calibration curve for the ferrite meter. Since the only magnetic phase that forms in 304 type of stainless steel after melting is δ-ferrite, the ferrite meter readings were taken as a measure of δ-ferrite formed in the material after laser remelting.

### 2.7 IGC Test

The ASTM A 262 practice C (Huey) test (Ref 14) was used to assess the susceptibility of the material to IGC. The test was carried out for five successive periods (each period of 48 h duration) in boiling 65% $HNO_3$. For the as-received material (heat B), the test was stopped after three periods because the corrosion rate was quite high. Three samples were tested for each heat-treated condition and the corrosion rate after the test was expressed as the average value of the three samples. ASTM specifies that for products showing end-grain pitting (e.g., bar, wire, and tubular products); the sample should be proportioned such that the area of exposed cross-section should not exceed half the total exposed area of the sample. The sample size was taken such that the cross-sectional (transverse) area was 20% of the total surface area. The IGC tests were also done on the laser-treated and weld deposit materials. For the laser-treated materials, samples of size 30 mm width were cut from both the rings of heats A and B, while for the weld deposit ring of heat A sample width size was 20 mm. In these cases, the cross-sectional area was 15% of the total exposed surface area. In order to identify the attack after exposure to the practice C test, the longitudinal section of the samples were mounted, polished and electroetched in 10% oxalic acid solution for a few seconds.

### 2.8 SEM-EDS Analysis

The corrosion attack after practice C was also observed using SEM. The inclusions present in the materials were chemically analyzed using SEM-EDS by taking line scans for different elements (Fe, Cr, Mn, S, and O) across the inclusion. In order to check whether flow lines are responsible for the intergranular attack, EDS analysis was performed by taking Fe, Cr, Si, and P line scans from the matrix to a point within the flow lines.

## 3. Results and Discussions

Both the heats of the as-received pipes were in the solution-annealed form. The microstructure after electrochemical etching in oxalic acid showed a step structure according to the classification of microstructures described in A262, practice A of ASTM (i.e., no chromium carbide precipitation or chromium depletion regions at grain boundaries). The microstructures obtained from the longitudinal and transverse sections (or end face) of heat B are shown in Fig. 1. Heat A also showed similar microstructure and the ASTM grain-size number was 6. The microstructure in the longitudinal section showed numerous small, dark, elongated stringers along the direction of cold working. This indicates the presence of inclusions, which are aligned along the direction of cold working and are of thin, stringer type. Apart from the inclusions, heavy flow lines are also visible in the material, which are again running along the direction of working. Generally, these heavy flow lines are present in the material when the solution annealing is not properly carried out. However, in the transverse section heavy end-grain pitting was observed in both the heats A and B. The end-grain pits are easily distinguished from etch pits by its total black appearance (Ref 14).

Figure 2a shows the inclusion in heat B across which the line scans of different elements was done using EDS in an SEM. The corresponding line scans for Fe, Cr, Mn, and S are shown in Fig. 2b. Since, variation in oxygen was not detected across the inclusion; its line scan has not been included in the figure. It can be seen from the result that the inclusions contain mainly Mn and S, hence these inclusions were manganese sulfide type inclusions.

Single loop EPR tests were carried out to quantitatively measure the degree of sensitization. The tests were done on both the longitudinal and transverse sections. Figure 3 shows the single loop EPR reactivation curves for both the heats (A and B) and the $P_a$ value for the respective samples are also indicated. The EPR reactivation loops were much bigger for the transverse section compared to the longitudinal section for both the heats. The same is true for the $P_a$ values, thus clearly indicating high-DOS or heavy corrosion attack in the transverse section. Although the samples had a ''step'' microstructure, i.e., no sensitization in the grain boundary area, nevertheless the $P_a$ value for heat A (which is ~6) and for heat B (which is ~20) was very high which are comparable to that for the ditch structure of an austenitic stainless steel ($P_a$ value > 5) (Ref 16). This is due to the morphology of heavy stringers type of

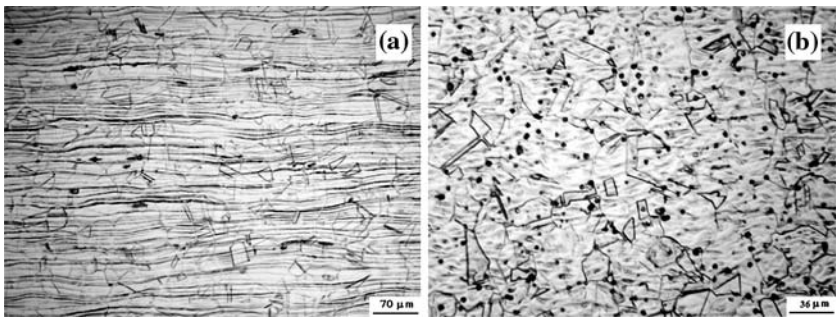


**Fig. 1** Microstructure of as-received sample of heat B in the (a) longitudinal section and (b) transverse section after ASTM A 262 practice A

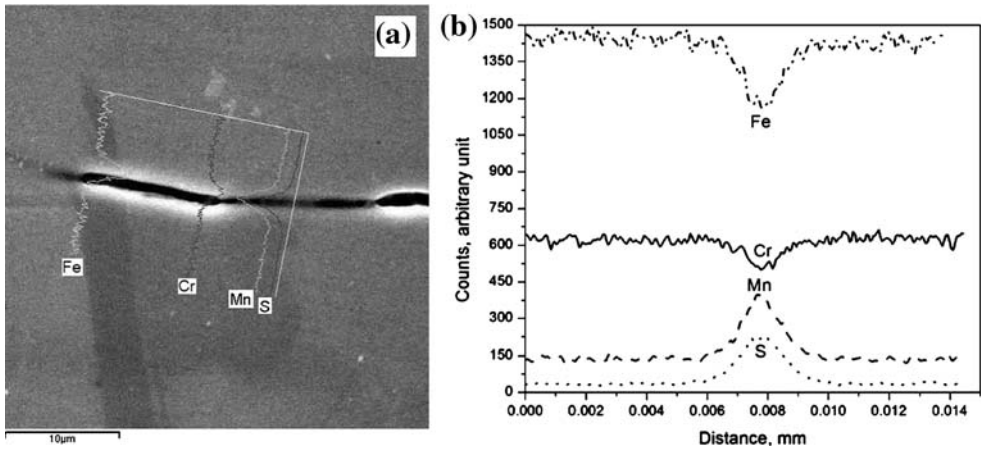


**Fig. 2** The as-received sample of heat B showing (a) the inclusion across which the line scans were done and (b) the corresponding line scans of Fe, Cr, Mn, and S showing the high counts of Mn and S in the inclusion

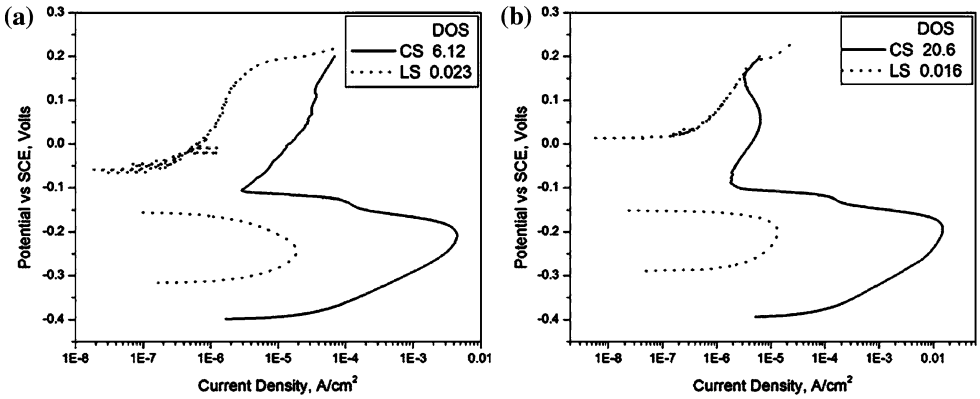


**Fig. 3** The single loop EPR curves of as-received samples of (a) heat A and (b) heat B on both the longitudinal and transverse (cross) sections showing higher-reactivation loop for the transverse sections. The $P_a$ value (C/cm$^2$) of each sample is also indicated. CS indicates cross section and LS indicates longitudinal section

inclusions present in the material. The stringer type inclusions extend deep into the transverse section and get dissolved from the transverse or end faces causing corrosion attack in the base metal in contact with the corrosive solution present inside the grooves. In the case of longitudinal section, the inclusions are only 2-3 μm deep. Even if the inclusions are dissolved during the EPR test, it does not initiate any corrosion attack in the base metal and hence very low $P_a$ value was observed. It should be emphasized that though the $P_a$ values measured from the EPR test are high, the reactivation current is mainly from the dissolution of inclusions and not due to sensitization.

One of the methods that have been used in the present study to control/minimize the end-grain corrosion was solution annealing of the material. Solution annealing is known to homogenize the structure of the material. Therefore, it should minimize the end-grain corrosion of the material occurring due to chemical inhomogenity. The temperature and time for the heat treatment was selected to minimize grain growth while permitting elemental diffusion to take place for homogenization of elemental segregation at flow lines. Three different solution annealing heat treatments were done on the samples of heat A. The susceptibility to IGC of these heat-treated samples together with the as-received sample was carried out by ASTM A 262 practice C. The value of IGC rate (in mils per year (mpy) and in mm/year) of each sample after five periods of practice C is shown in Fig. 4. After the test, the longitudinal section of each samples were examined under optical microscope in both as-polished and etched condition and the microstructures are shown in Fig. 5. The normally acceptable corrosion rate for 304L material in annealed condition is 0.457 mm/year (Ref 17). The IGC rate for the as-received sample (1.858 mm/year) was the highest, which is well above the acceptable limit. The microstructure after the test shows a number of pitting type of attack starting from the transverse or end face of the sample and advancing deep into the base metal. Since the area at the end face is attacked for longer duration, the corrosion attack is more severe or wide at the end faces. At the farthest point from the end faces, the attack is the least (narrow) and its intergranular nature is clearly evident. The heat treatment at 950 °C for 30 min does not improve the resistance to end-grain corrosion and the corrosion rate (1.718 mm/year) is almost same as that of the as-received material. The heat treatment at 1000 °C for 30 min leads to substantial decrease in the corrosion rate of the sample in practice C, the corrosion rate (0.783 mm/year) is almost half to that of the as-received material. However, the corrosion rate is still above the acceptable limit for the annealed material. The microstructures of both the above heat-treated samples showed the same type of corrosion attack as observed

in the as-received condition after practice C, and is shown in Fig. 5. It is clear from Fig. 5 that the corrosion is intergranular in a nitric acid environment. The attack had started from the end faces and is intergranular despite absence of sensitization at grain boundaries. The sample heat-treated at 950 °C for 90 min showed drastic decrease in the corrosion rate (0.439 mm/year), which is also below the acceptable limit. There was no increase in the grain-size of the material after the heat treatments at 950 °C for either 30 or 90 min and the ASTM grain-size number was same as that of the as-received material (equal to six). However, for the sample heat-treated at 1000 °C for 30 min the ASTM grain-size number has increased to five.

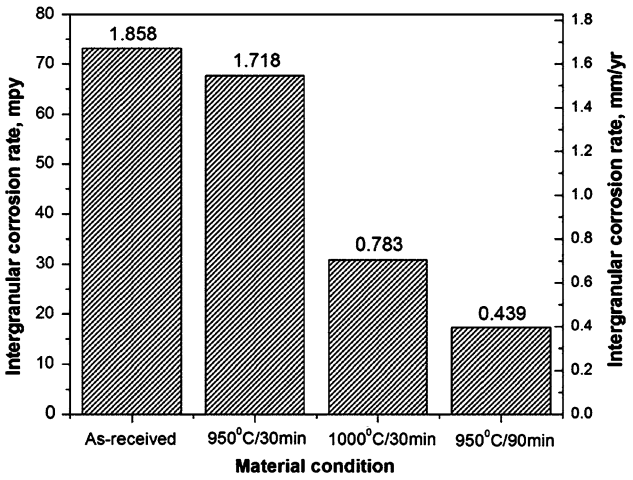


**Fig. 4** Corrosion rate of heat A in different heat-treated conditions as per ASTM A 262 practice C. The corrosion rates are in mpy (mils per year) and mm/year on the left and right *Y*-axis, respectively

In practice C, chromium-depleted areas, chromium carbide, and non-metallic inclusions are attacked. Since the microstructure of the as-received sample of heat A did not show any carbide precipitation at the grain boundary, the high-corrosion rate observed in practice C is attributed to the presence of elongated MnS inclusions and/or segregation of certain elements such as Cr, Si, and P along the flow lines. No oxide layer exists between the sulfide inclusion and the metal matrix. Therefore, dissolution of stringer types of sulfide inclusions takes place from the exposed end (cross-sectional) faces. This causes accumulation of $Cr^{+6}$ ions in the cavities that formed due to dissolution of inclusions (Ref 10), as-well-as a fresh metal surface are exposed to the corrosive environment. This makes the environment within the dissolved inclusions even more aggressive and the high-energy grain boundaries start corroding leading to IGC (Ref 10). However, chromium depletion caused by segregation of chromium along flow lines also leads to such heavy attack. Therefore, initiation of corrosion is due to dissolution of inclusions but the propagation is accelerated by manufacturing related flow lines and chromium segregation along it. This form of corrosion occurs specifically in a strongly oxidizing environment. The depletion of chromium around the inclusions may be the other reason for enhanced attack observed in practice C. It has been reported recently (Ref 18) that sulfide inclusions may have a thin layer of chromium depletion around them and that is responsible for the pitting attack in stainless steels. However, this finding has not been confirmed by other studies (Ref 19) and remains to be proven.

The solution annealing heat treatment at 950 °C for 90 min improved the resistance to end-grain corrosion of heat A without any increase in the grain-size of the material. To confirm this result, the same heat treatment was done on the sample of heat B and the susceptibility to IGC was compared with that of the as-received sample after ASTM A 262 practice C. The results of practice C are shown in Table 2. The IGC rate

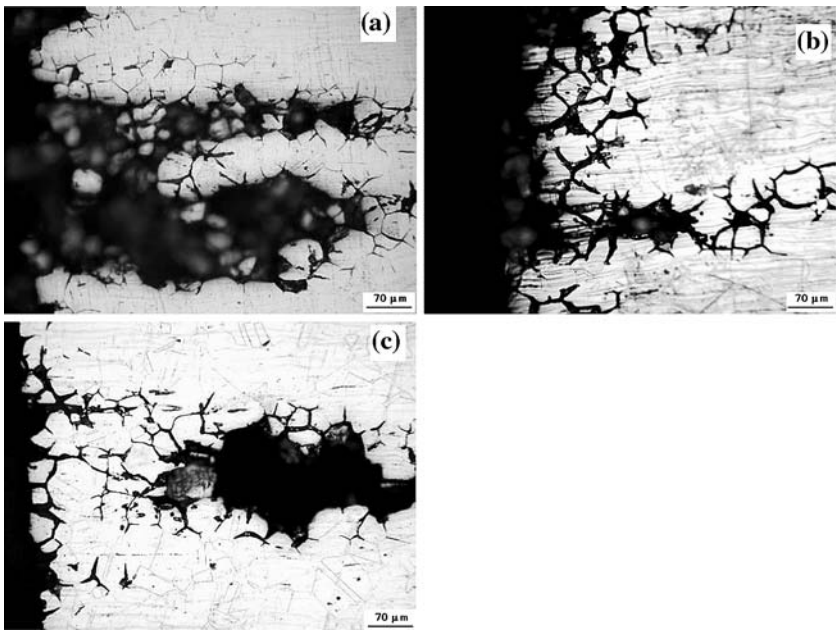


**Fig. 5** The microstructure in the longitudinal section of heat A after practice C in the (a) as-received, (b) 950 °C/30 min, and (c) 1000 °C/30 min condition showing corrosion attack starting at the end face which leads to intergranular corrosion

for the as-received material was very high and the test was stopped after three periods. Again this high-corrosion rate observed for the as-received sample of heat B after practice C is due to the presence of heavy inclusions and flow lines present in the material. Figure 6a shows the longitudinal section of the as-received sample of heat A after practice C. Heavy corrosion attack can be seen starting from the end faces of the sample and leading to IGC, which is similar to the attack observed for samples of heat A. Figure 6b also shows the SEM micrograph of the same attacked area, which clearly shows the falling of grains after practice C. For the heat-treated sample at 950 °C for 90 min, the corrosion rate after practice C was found to be very low (0.246 mm/year). The observed corrosion rate is well below the acceptable limit of 0.457 mm/year for solution-annealed material. The microstructure of the heat-treated sample did not show any corrosion attack after the test.

To confirm whether homogenization of different elements (such as Cr, Si, P, etc.) in the flow line regions are responsible for improved resistance to end-grain corrosion, line scans of Cr, Fe, Si, and P were performed across the flow lines on the as-received and 950 °C/90 min heat-treated samples of heat B after ASTM A 262 practice C. The results are shown in Fig. 7 for the as-received sample and Fig. 8 for the heat-treated sample at 950 °C for 90 min. The line profiles in Fig. 7 show the distribution of Cr, Si, and P along the flow lines in the as-received material. Although, the exact Cr concentration within the flow lines, could not be measured, a variation in chromium concentration could be detected across the flow lines (Fig. 7). The variation in Cr, Si, and P for the heat-treated sample (Fig. 8) was much less compared to that for the as-received sample (Fig. 7). This is due to the homogenization of elements taking place at the higher temperature due to faster diffusion. Thus solution annealing at 950 °C for 90 min is an effective method to minimize the end-grain corrosion of austenitic stainless steels. This solution annealing does not change the number of inclusions present in the material; however, it increases the resistance to end-grain corrosion. It reduces the segregation of elements present at the flow lines. There is reduction in the variation of chromium concentration across the flow lines after the solution annealing treatment as shown in Figs. 7 and 8.

**Table 2 Corrosion rates measured after ASTM A 262 practice C for 304L samples of heat B after the 5th period**

| Sample condition | Corrosion rate, mm/yr |
|---|---|
| As-received | 3.5763 (after 3 periods) |
| 950 °C/90 min | 0.2464 |

Laser surface remelting was carried out on both the heats of A and B in the as-received condition. The ferrite meter measurement on these samples showed formation of δ-ferrite in the melt pool, which were in the range of 0.4-0.5%. The melted pool showed a modified dendritic structure. Compared with the typical dendritic structure, the substructures of the melted layer were greatly refined. This is due to the very fast rate of cooling in the laser-melted pool. Figure 9 shows the microstructure of heat B at the interface between the laser melt pool and the wrought base metal. The semi-continuous network of δ-ferrite phase in austenite matrix is clearly evident in the laser-melted layer. The δ-ferrite content in the melted zone was observed to increase toward the boundary between the melted zone and the base metal. There is also removal and/or redistribution of elongated MnS inclusions to spherical shape, as evident in the microstructure (Fig. 9). These results confirm the results of an earlier reported study (Ref 20, 21).

Samples of laser-treated material of both the heats (A and B) were subjected to practice C to find out the susceptibility of these materials to IGC. The results are shown in Table 3. The corrosion rate of the laser-treated samples of both the heats was much lower than the corrosion rate observed for samples in their as-received condition. The longitudinal sections of the samples after practice C were examined under an optical microscope and did not show any corrosion attack. The reason for the improved resistance to end-grain corrosion of laser-treated materials is clearly due to the modification of microstructure of the end faces after laser remelting. The elongated inclusions and segregation of Cr, Si, and P along the flow lines, which are mainly responsible to end-grain corrosion, get eliminated along with the aligned wrought microstructure after laser remelting. This modified structure remains in contact with the corrosive environment. Pan et al. (Ref 13) has proposed a similar theory for improvement of IGC resistance of sensitized SS 321 after laser surface remelting, i.e., the redistribution and/or removal of initial carbides. The redistribution of carbides from the clustered to the dispersed or even complete dissolution in the laser-melted layer leads to a modified microstructure with an insignificant chromium-depleted zone, thus leading to the improvement in IGC resistance. Another factor that could be

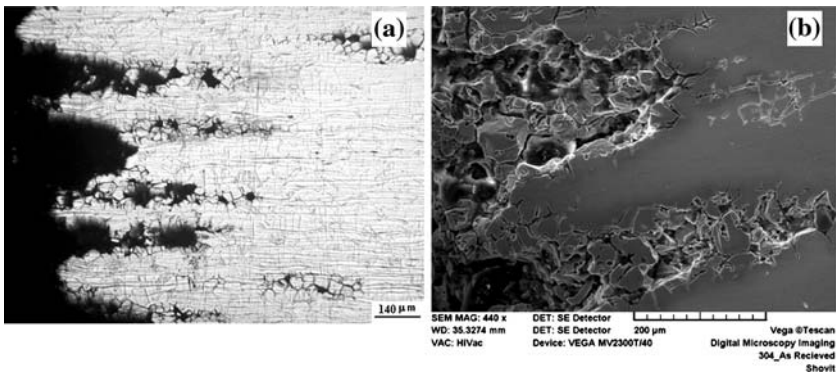


**Fig. 6** The microstructure of as-received sample of heat B in the longitudinal section after practice C showing heavy corrosion attack starting from the end faces, and (b) SEM micrograph of the same attacked area. The grains falling out are clearly visible

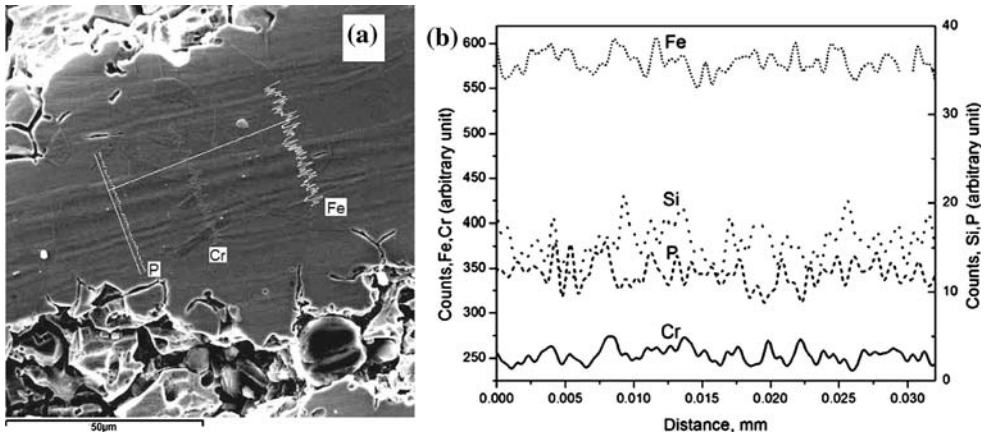


**Fig. 7** As-received sample of heat B after practice C showing (a) flow lines across which EDS line profile was performed, and (b) the corresponding line profile of Fe, Cr, Si, and P

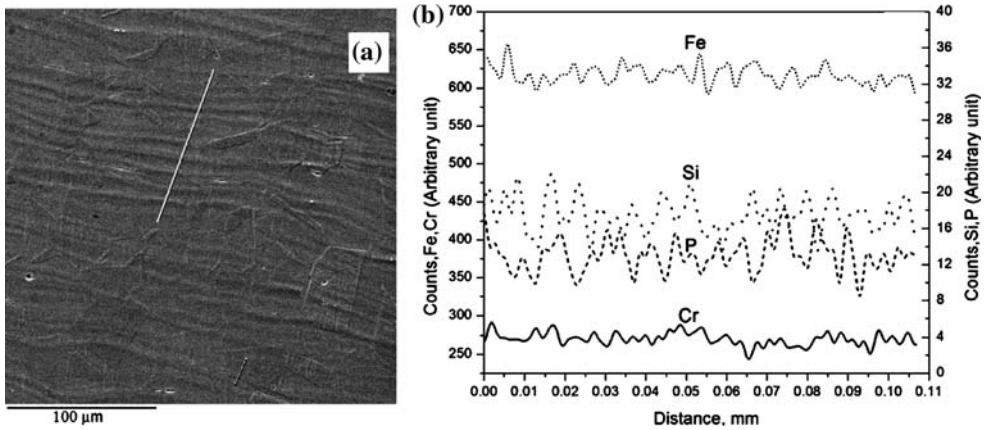


**Fig. 8** The sample of heat B heat-treated at 950 °C for 90 min after practice C showing (a) flow lines across which the EDS line profile was performed, and (b) the corresponding line profile of Fe, Cr, Si, and P

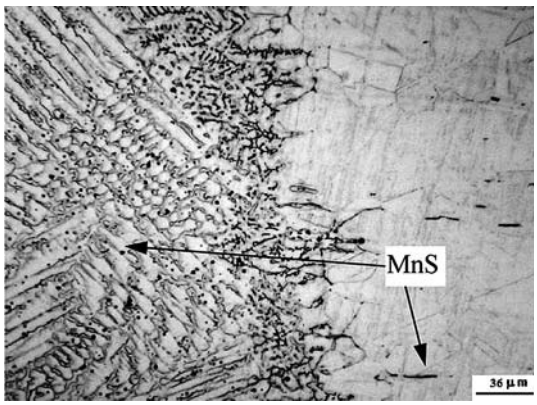


**Fig. 9** The microstructure of laser surface remelted sample of heat B after light etching in oxalic acid, showing the interface between the laser melt pool and the wrought structure base metal. Different morphologies of MnS inclusions in the base material and in the laser-remelted region can be seen

contributing for the increase of IGC resistance is the presence of δ-ferrite in the melt pool, which makes the austenite grain network discontinuous. It was reported that such a structure is advantageous to improve the IGC resistance, as it eliminates the continuous pathway for IGC to proceed (Ref 22).

**Table 3 Corrosion rates measured after the 5th period of ASTM A 262 practice C for 304L samples of heats A and B after laser surface remelting**

| Sample condition | Corrosion rate, mm/yr |
|---|---|
| Laser treated, Heat A | 0.185 |
| Laser treated, Heat B | 0.208 |

The weld deposition on the end faces of the ring of heat A was carried out using SS 308L material. The weld deposit showed a typical cast structure and was free from inclusions. Figure 10 shows the interface between the weld deposit and the base metal in the longitudinal direction. The sample with weld deposition on both the end faces was examined for IGC test according to practice C. The corrosion rate after five periods was found to be 0.161 mm/year well within the acceptable limit and was much lower compared to the corrosion rate of the sample in the as-received condition. Weld deposition on the end faces masks the susceptible material (to end-grain corrosion) with a more corrosion resistant material. Therefore, the cross sections (the susceptible material) of the sample are not

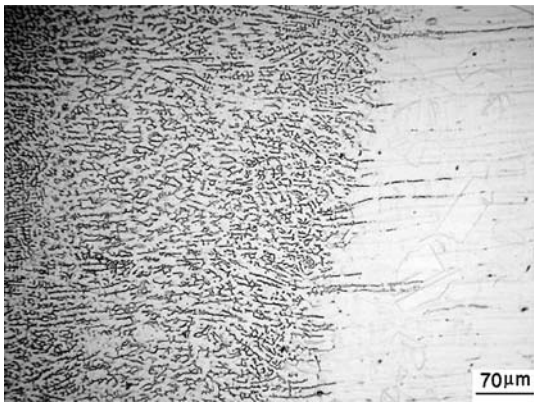


**Fig. 10** The microstructure of the weld deposit sample of heat A, showing the interface between the deposited metal and the base metal

exposed to the corrosive environment. This helps in increasing the corrosion resistance of the component.

Surface alloying with Cr, Mo, etc., on the cross-sectional surfaces is the other possible method that can be used for this purpose. A practical method to avoid/minimize end-grain corrosion in operating plants is welding of a better quality material of the same grade on the exposed cross-sectional surfaces. This is an easy method that can be applied in plants. The heat-treatments technique to control end-grain corrosion suggested in this study too can be used in plant applications. In this case only the last section of the tube/tubular product to be welded (that has the exposed cross-sectional surfaces) only needs to be heat-treated.

## 4. Conclusions

Based upon the corrosion tests in boiling nitric acid, it has been shown that stringer-shaped inclusions of manganese sulfide type and segregation of chromium along flow lines are the main reasons for end-grain corrosion in austenitic stainless steels used in highly oxidizing solutions, e.g., boiling nitric acids. It has been demonstrated that the controlled solution annealing heat treatment, laser surface remelting, and weld deposition with a corrosion resistant material on the exposed faces are effective methods to improve the resistance to end-grain corrosion of austenitic stainless steels. A simple method to avoid/minimize end-grain corrosion in operating plants is welding of a better quality material of the same grade.

### Acknowledgments

The authors thank Mr. B. P. Sharma, Associate Director (S), Materials group, Bhabha Atomic Research Centre, Mumbai for his keen interest in our work and permission to publish this paper. The authors thank the help received for SEM and EDS examination from Dr. Shobhit Bhattacharya of Bhabha Atomic Research Centre, Mumbai.

### References

1. R.L. Cowan and C.S. Tedmon, *Intergranular Corrosion of Alloys: Advances in Corrosion Science and Technology*, vol. 3, M.G. Fontana and R.W. Staehle, Eds., Plenum Press, New York, NY, 1973, p 293
2. A.J. Sedricks, *Corrosion of Stainless Steels*, 2nd ed., John Wiley and Sons, New York, NY, 1996, p 13
3. V. Kain, R.C. Prasad, and P.K. De, Testing Sensitization and Predicting Susceptibility to Intergranular Corrosion and Intergranular Stress Corrosion Cracking, *Corrosion*, 2002, **58**, p 15–38
4. C.L. Briant, R.A. Mulford, and E.L. Hall, Sensitization of Austenitic Stainless Steels, 1. Controlled Purity Alloys, *Corrosion*, 1982, **38**(9), p 468–477
5. V. Kain, S.S. Shinde, and H.S. Gadiyar, Mechanism of Improved Corrosion Resistance of Type 304L Stainless Steel, Nitric Acid Grade, in Nitric Acid Environments, *J. Mater. Eng. Perf.*, 1994, **3**(6), p 699–705
6. V. Kain and P.K. De, Controlling Corrosion in the Back End of Fuel Cycle Using Nitric Acid Grade Stainless Steel, *Inter. J. Nuclear Energy Sci. Technol.*, 2005, **1**(2–3), p 222–231
7. R.D. Shaw, Corrosion Prevention and Control at Sellafield Nuclear Fuel Reprocessing Plant, *Br. Corros. J.*, 1990, **25**, p 97–107
8. V. Kain, P. Sengupta, P.K. De, and S. Banerjee, Case Reviews on the Effect of Microstructures on the Corrosion Behavior of Austenitic Alloys for Processing and Storage of Nuclear Waste, *Metall. Mat. Trans. A*, 2005, **36A**, p 1075–1084
9. G.O.H. Whillock, B.F. Dunnett, and M. Takeuchi, Techniques for Measuring the End-Grain Corrosion Resistance of Austenitic Stainless Steels, *Corrosion*, 2005, **61**(1), p 58–67
10. V. Kain, S.S. Chouthai, and H.S. Gadiyar, Performance of AISI 304L Stainless Steel with Exposed End Grain in Intergranular Corrosion Tests, *Brit. Corr. J.*, 1992, **27**(1), p 59–65
11. J.Y. Jeng, B.E. Quayle, P.J. Modern, W.M. Steen, and B.D. Bastow, Laser Surface Treatments to Improve the Intergranular Corrosion Resistance of 18/13/Nb and 304 in Nitric Acid, *Corr. Sci.*, 1993, **35**(5–8), p 1289–1296
12. J. Stewart and D.E. Williams, The Initiation of Pitting Corrosion on Austenitic Stainless Steel: On the Role and Importance of Sulphide Inclusions, *Corr. Sci.*, 1992, **33**(3), p 457–474
13. Q.Y. Pan, W.D. Huang, R.G. Song, Y.H. Zhou, and G.L. Zhang, The Improvement of Localized Corrosion Resistance in Sensitized Stainless Steel by Laser Surface Remelting, *Surf. Coat. Tech.*, 1998, **102**, p 245–255
14. "ASTM Designation A-262, Practice B" in Annual Book of ASTM Standards, ASTM, Philadelphia, PA, 2005
15. "ASTM Designation G-108" in Annual Book of ASTM Standards, ASTM, Philadelphia, PA, 2005
16. A.P. Mazidi and M.A. Streicher, Potentiodynamic Reactivation Method for Detecting Sensitization in AISI 304 and 304L Stainless Steels, *Corrosion*, 1984, **40**(8), p 393–408
17. M.H. Brown, Behavior of Austenitic Stainless Steels in Evaluation Tests for the Detection of Susceptibility to Intergranular Corrosion, *Corrosion*, 1974, **30**(1), p 1–12
18. M.P. Ryan, D.E. Williams, R.J. Chater, B.M. Hutton, and D.S. McPhail, Why Stainless Steel Corrodes, *Nature*, 2002, **415**, p 770–774
19. Q. Meng, G.S. Frankel, H.O. Colijn, and S.H. Goss, High-Resolution Characterization of the Region Around Manganese Sulfide Inclusions in Stainless Steel Alloys, *Corrosion*, 2004, **60**(4), p 346–355
20. O.V. Akgun and O.T. Inal, Laser Surface Melting and Alloying of Type 304L Stainless Steel. Part I Microstructural Characterization, *J. Mater. Sci.*, 1995, **30**, p 6097–6104
21. O.V. Akgun and O.T. Inal, Laser Surface Melting and Alloying of Type 304L Stainless Steel. Part II Corrosion and Wear Resistance Properties, *J. Mater. Sci.*, 1995, **30**, p 6105–6112
22. J. Stewart, D.B. Wells, P.M. Scott, and A.S. Brandsen, The Prevention of IGSCC in Sensitized Stainless Steel by Laser Surface Melting, *Corrosion*, 1990, **46**(8), p 618–621